Second-order harmonic and combination modes in graphite, single wall carbon nanotube bundles, and isolated single wall carbon nanotubes

V. W. Brar[a], Ge. G. Samsonidze[b], M. S. Dresselhaus[a,b], G. Dresselhaus [c]
[a] *Department of Physics,* [b] *Department of Electrical Engineering and Computer Science,*
[c] *Francis Bitter Magnet Laboratory, Massachusetts Institute of Technology, Cambridge, MA 02139-4307*

R. Saito
Department of Electronic-Engineering, University of Electro-Communications, Tokyo, 182-8585, Japan

A. K. Swan,[d] M. S. Ünlü,[d], B. B. Goldberg[d,e]
[d] *Electrical and Computer Engineering Department,*
[e] *Department of Physics, Boston University, Boston, MA 02215*

A. G. Souza Filho[f], A. Jorio[g]
[f] *Departamento de Física, Universidade Federal do Ceará, Fortaleza-CE, 60455-760, Brazil*
[g] *Instituto de Nanociências e Departamento de Física,*
Universidade Federal de Minas Gerais, Belo Horizonte, MG, 30.123-970 Brazil
(Dated: February 26, 2002)

We report a study of second-order combination and overtone modes in highly ordered pyrolytic graphite (HOPG), in single wall carbon nanotube (SWNT) bundles, and in isolated SWNTs. We found both dispersive and non-dispersive Raman bands in the range 1650–2100 cm^{-1}, and we show that the appearance and frequency vs. laser energy E_{laser} behavior of these features are in agreement with predictions from double resonance Raman theory. In the case of SWNTs, these second-order bands depend on the one-dimensional structure of SWNTs, and, at the single nanotube level, the spectra vary from tube to tube, depending on tube diameter and chirality, and on the energy of the van Hove singularity relaative to E_{laser}.

PACS numbers: 78.30.Na; 78.66.Tr

I. INTRODUCTION

Carbon materials are very important for science and technology, appearing in many different forms, such as highly ordered pyrolytic graphite (HOPG), activated carbons, carbon fibers, and other forms important to our industrial society [1]. The recently discovered carbon nanotubes show remarkable signs of applicability for a number of future, technological applications, artificial muscles [2], scanning probes [3], and electron field emitters [4]. They are also unique in their ability to model one-dimensional systems, the electronic and vibrational properties varying from tube to tube on the basis of their diameters and chiralities [5, 6].

Raman spectroscopy has already proven to be a powerful technique to study carbon materials [1], including single wall carbon nanotubes (SWNTs) through the diameter selective resonance Raman effect [7, 8]. It has been known for some time [1] that graphite-related materials exhibit a rich Raman spectra, with several first- and second-order features, disorder-induced bands, some of them being dependent on laser excitation energy E_{laser}. However, many of these features remained unexplained for a long time. It is only recently that the appearance of these features and their dependence on E_{laser} were explained as due to a double resonance process that enhances the scattering of light by certain modes in the interior of the Brillouin zone ($q \neq 0$) of graphite-related materials [9–11].

In the present work we study weak Raman features observed in the frequency range 1650–2100 cm^{-1} in graphite-related materials (i.e., HOPG, SWNT bundles and isolated SWNTs) and we show that these features are related to overtones and combination modes of the several phonon branches in graphite, as predicted by double resonance theory [9, 10].

In particular, we consider here a multi-featured band at about 1750 cm^{-1}. This band was previously observed, but until now unassigned, in HOPG [12], in irradiated graphite [13], and it is also observed in SWNT bundles, where it was tentatively assigned as a combination mode of the G band and the radial breathing mode (RBM) [14]. We assign this feature in the present work to an overtone of the infrared-active out-of-plane (oTO) mode at 867 cm^{-1} in graphite. The oTO mode has been observed in Raman spectra taken along the broken edges of HOPG [15] and in SWNTs [16]. In addition, we report a very highly dispersive mode at higher frequencies (around 1950 cm^{-1}) that has previously been reported for SWNT bundles [17], and we tentatively identify this mode as a combination of the longitudinal optic (LO) and longitudinal acoustic (LA) modes, namely (LO+LA). The results for both the features around 1750 cm^{-1} and the feature around 1950 cm^{-1} provide experimental evidence for the predictions of double resonance Raman theory for overtones and combinations of modes [9, 10]. In the case of

isolated SWNTs, the multi-featured band at 1750 cm^{-1} shows a richer behavior than in HOPG (and is more complicated than the D-band and the G'-band in isolated SWNTs [18, 19]), varying from tube to tube, thus suggesting a strong dependence on the one-dimensional structure of SWNTs.

II. EXPERIMENTAL DETAILS

Raman spectra for HOPG and isolated SWNTs were acquired under ambient conditions, using a single monochromator Renishaw 1000B spectrometer equipped with a cooled Charge Coupled Device (CCD) detector and notch filters, in a back scattering configuration. The excitation laser line $E_{\mathrm{laser}} = 2.41\,\mathrm{eV}$ from an Ar laser was used for HOPG and for the isolated SWNTs. Data from SWNT bundles ($d_t = 1.49 \pm 0.20\,\mathrm{nm}$ determined from transmission electron microscope measurements) obtained with the laser excitation energy $E_{\mathrm{laser}} = 1.58$, 1.96, 2.41 and 2.71 eV by Brown et al. [17] were used in our analysis to study the dependence of the various features on E_{laser}.

Isolated SWNTs were prepared by a chemical vaporization deposition (CVD) method on a Si/SiO_2 substrate containing nanometer size iron catalyst particles [20, 21]. Atomic force microscopy (AFM) was used to characterize the isolated SWNT sample, showing that the SWNTs ranged in diameter from 1 to 3 nm, and had lengths ranging from a few hundred nm up to 2μm. The AFM images showed a very low SWNT density ($\sim$40 nanotubes/100$\mu\mathrm{m}^2$), and showed that most of the SWNTs did not touch one another. We measured the Raman spectra from more than 100 isolated SWNTs resonant with $E_{\mathrm{laser}} = 514.5\,\mathrm{nm}$ (2.41 eV). Of all the spectra taken, the spectra from only 51 tubes were used to conduct this study, since the $\sim 1750\,\mathrm{cm}^{-1}$ Raman feature was not observed in many spectra. Of these 51, not all tubes were used in each part of the study, since the spectra from some tubes did not show an observable radial breathing mode (RBM) feature, which we used for the nanotube diameter determination (using the relation $d_t = 248/\omega_{\mathrm{RBM}}$) and for the tentative (n, m) assignments based on Ref. 21.

III. RESULTS AND DISCUSSION

A. General Results

The top three traces in Fig. 1 show Raman spectra between 1650 cm^{-1} and 2100 cm^{-1} from HOPG, SWNT bundles, and an isolated SWNT, using $E_{\mathrm{laser}} = 2.41\,\mathrm{eV}$. This laser line excites semiconducting SWNTs predominantly, considering the SWNT diameters and diameter distributions contained in the various samples. The G-band feature (not shown) is used as a signature to distinguish whether the nanotubes are semiconducting or metallic for the various samples [22]. HOPG shows a single Lorentzian G line at 1582 cm^{-1}, while SWNTs show several G-band peaks due to their cylindrical structure and to zone folding effects [7]. The main difference in the G-band spectra between SWNT bundles and isolated SWNTs is in the linewidths Γ_G, which are smaller for isolated SWNTs than for SWNT bundles [23]. A very weak (or unobservably small) D-band intensity for most of the observed nanotubes indicates a high degree of crystallinity of the probed samples.

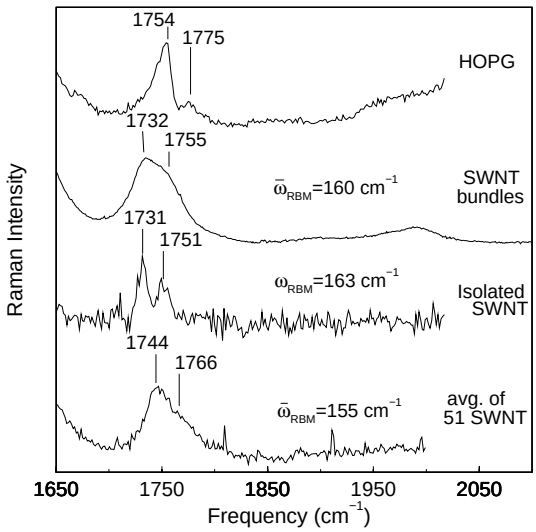

FIG. 1: Raman spectra from HOPG, SWNT bundles, an isolated SWNT, and an average over 51 isolated SWNTs where the average is taken by summing the 51 spectra, all normalized to a common spectral feature. All of these spectra were excited at laser energy $E_{\mathrm{laser}} = 2.41\,\mathrm{eV}$. The frequencies of some peaks are indicated in cm^{-1}, and $\overline{\omega}_{\mathrm{RBM}}$ denotes the average radial breathing mode frequency for the SWNT bundle and for the sum of the 51 spectra for isolated SWNTs.

All the spectra in Fig. 1 show the presence of a multi-featured band at about 1750 cm^{-1} whose origin has not yet been assigned in the literature. (We here call this band the M band reflecting the two-peak visual shape of this band). This M band in HOPG and for the isolated (15,7) SWNT (second trace from the bottom in Fig. 1, diameter $d_t = 1.52\,\mathrm{nm}$) clearly shows two components. We therefore conclude that a single (n, m) nanotube can give rise to the two peak structure also observed in HOPG. The lowest trace in Fig. 1 shows the average of this M feature in the summation of Raman spectra taken from 51 isolated SWNTs (mean diameter = 1.6 nm), and we can fit the resulting asymmetric lineshape with two Lorentzian peaks. The asymmetric lineshape in Fig. 1 for SWNT bundles is likewise fit to two Lorentzian peaks. All four examples of this M band in Fig. 1 exhibit a similar splitting of $\sim 20\,\mathrm{cm}^{-1}$ at $E_{\mathrm{laser}} = 2.41\,\mathrm{eV}$, but the average M-band frequencies are somewhat upshifted (or downshifted) from each other, probable due to the presence or absence of bundle interactions and curvature ef-

TABLE I: Frequencies ω_M^+ and ω_M^-, frequency difference $\Delta\omega_M$ between ω_M^+ and ω_M^- and the (averaged) diameters d_t for the spectra shown in Fig. 1.

	HOPG	SWNTs		
		bundle	(15,7)	avg. 51 NTs
ω_M^-	1754	1732	1731	1744
ω_M^+	1775	1755	1751	1766
$\Delta\omega_M$	21	23	20	22
d_t	∞	1.55*	1.52	1.6

*1.55 nm denotes the averaged diameter distribution of the SWNTs resonant with $E_{\rm laser} = 2.41$ eV, deduced from the RBM feature in the SWNT bundle sample [14].

fects. A summary of this analysis is in Table I for the upper (ω_M^+) and lower (ω_M^-) frequency components and for the splitting $\Delta\omega_M = \omega_M^+ - \omega_M^-$. For all nanotubes in Table I, d_t is determined from the radial breathing mode frequency, using the relation $\omega_{\rm RBM} = 248/d_t$ [21], and averaged values are given for SWNT bundles and for the summation spectrum from the 51 isolated SWNTs.

Previously, this M feature was tentatively assigned to a combination mode of the G band and RBM features ($\omega_G + \omega_{\rm RBM}$) [17]. However, as can be seen in Fig. 1, the presence of this feature in HOPG, which has no RBM, indicates that a different explanation for this feature is needed.

Another very weak feature can also be seen in the spectrum in Fig. 1 for HOPG and SWNT bundles above 1950 cm^{-1}. We will call this (LO + LA) feature LOLA, as explained later. Previously, this feature was tentatively assigned as a combination mode ($\omega_G + 2\omega_{\rm RBM}$). [17] Once again, a different explanation is needed, since this feature is observed also in HOPG. Furthermore, as shown in Ref. 17, this feature is strongly dispersive, in disagreement with the ($\omega_G + 2\omega_{\rm RBM}$) tentative assignment in Ref. 17, as we discuss below.

B. Mode Assignments

To help with the identification of the origin of the features near 1750 cm^{-1} (M) and near 1950 cm^{-1} (LOLA) in Fig. 1, an analysis of the dependence of the spectra on $E_{\rm laser}$ was carried out to determine the dispersion of these spectral features as $E_{\rm laser}$ is varied. Such information can be deduced from the spectra in Ref. 17 on SWNT bundles. Figure 2 shows that the M feature near 1750 cm^{-1} can be analyzed in terms of two components with frequencies ω_M^- and ω_M^+. A Lorentzian fit was therefore made of the several Raman features observed from 1650 to 2100 cm^{-1} from SWNT bundles, using different $E_{\rm laser}$ excitation lines. This figure shows that the lower frequency mode ω_M^- exhibits a weakly dispersive behavior (frequency ω_M^- shifting down by ~ 30 cm^{-1} as $E_{\rm laser}$ is

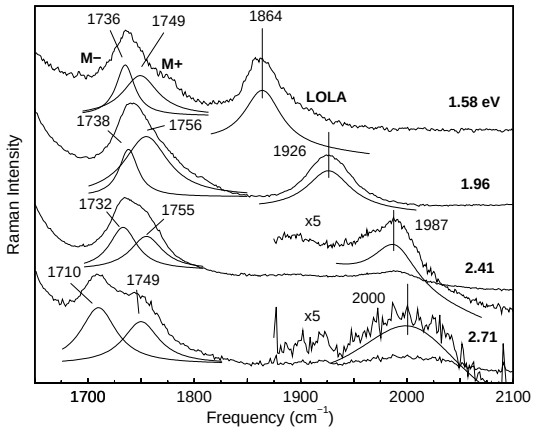

FIG. 2: Lorentzian fits of the Raman spectra taken at several $E_{\rm laser}$ values for the M feature near 1750 cm^{-1} and the highly dispersive LOLA feature observed at 1950 cm^{-1} in SWNT bundles, taken from Brown et al. [17]. Peak frequencies (cm^{-1}) and $E_{\rm laser}$ values (eV) are displayed.

varied from 1.58 eV to 2.71 eV), while the upper feature frequency ω_M^+ is basically independent of $E_{\rm laser}$. The higher frequency LOLA mode is highly dispersive and upshifts from 1864 cm^{-1} to 2000 cm^{-1} as $E_{\rm laser}$ varies from 1.58 eV to 2.71 eV, corresponding to a dispersion of 120 cm^{-1}/eV.

Well-known frequency dispersive modes in graphite-related materials are the disorder-induced D band, and its second-order feature, the G' band. Their appearance and dispersive behavior were recently explained as due to a double resonance process [10]. Saito et al. [9] subsequently applied the double resonance theory developed for the D/G' bands to all the phonon branches of graphite, and showed that many low intensity dispersive and non-dispersive features are expected to appear in the Raman spectra of graphite-related materials, reflecting the vibrational and electronic structure of the material. Although they only applied the double resonance theory to one-phonon processes explicitly, the corresponding mechanisms can be applied to two-phonon processes, giving rise to combination modes and overtones, like the G' band [9, 10]. As we discuss below, we propose here that the features observed between 1650 and 2100 cm^{-1} are overtones and combination modes related to graphite, as predicted by double resonance theory [9]. More specifically, the two features near 1750 cm^{-1} (M band) are attributed to overtones of the out-of-plane (oTO), infrared-active mode at 867 cm^{-1} in graphite [15], and the feature at $\sim$1950 cm^{-1} (LOLA band) is attributed to a combination of one phonon from the longitudinal optical branch (LO) plus one phonon from the longitudinal acoustic (LA) branch, LO+LA.

Figure 3(a) shows the phonon dispersion curves for graphite from the Γ-point to the K-point of the 2D graphite Brillouin zone from Ref. 9. Also plotted are the predicted dispersion relations for the second-order

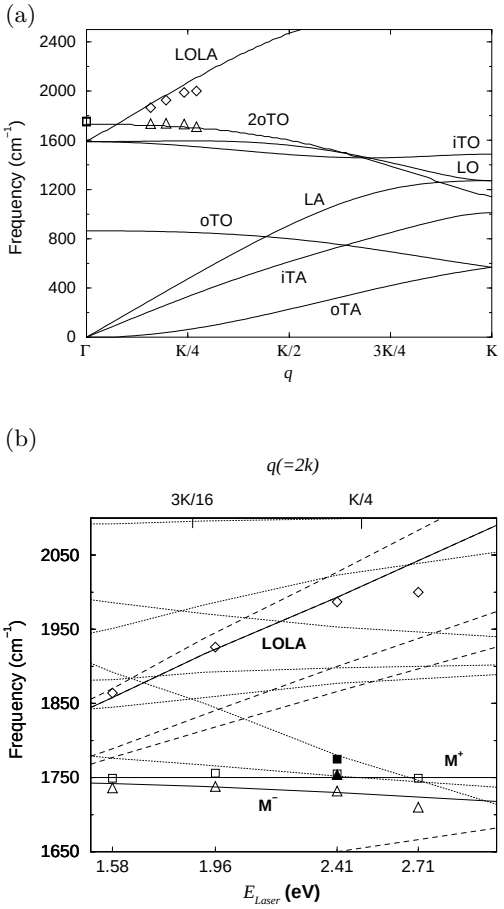

FIG. 3: (a) The phonon dispersion curves for graphite from the Γ-point to the K-point from Ref. 9. Also plotted are the predicted dispersion relations and experimental points for the second-order overtone of the out-of-plane optical (oTO) mode (related to the $M^{\pm}$ bands) and for the second-order combination LO+LA of the longitudinal optical (LO) and longitudinal acoustic (LA) modes (related to the LOLA band). (b) ω_M^-, ω_M^+ and $\omega_{\rm LOLA}$ frequencies vs. $E_{\rm laser}$ (lower scale) for the M bands and LOLA band. This figure corresponds to an expanded scale for (a). The corresponding $|q| \simeq 2|k|$ values for M^- and LOLA are plotted on the upper scale (the upper scale does not apply to the M^+ mode). The experimental results from SWNT bundles taken from Fig. 2 are represented by: ω_M^- (△), ω_M^+ (□), LOLA (◇). The solid curves represent the predicted frequencies of $\omega_M^{\pm}$ vs. $E_{\rm laser}$ upshifted by $20\,{\rm cm}^{-1}$, and the solid curve shows the predicted frequencies of $\omega_{\rm LOLA}$ vs. $E_{\rm laser}$. The dotted lines show all the other possible predicted combination and overtone modes in graphite associated with the K-point, while the dashed lines represent predicted combination and overtone modes from the Γ-point, according to double resonance theory [9].

overtone of the out-of-plane optical (oTO) mode (related to the $M^{\pm}$ bands for which the splitting between the M^+ and M^- bands is not resolved on this scale) and for the second-order combination mode corresponding to the (LO + LA) or LOLA band. The experimental points are plotted in Fig. 3(a) as a function of phonon wave vector q according to double resonance theory [9], as discussed in the next paragraphs. Note that the agreement between the experimental and theoretical frequencies for the overtone (M) and combination (LOLA) bands is very good.

Assuming that the M band is an overtone of the band near $\omega_{\rm oTO} = 867\,{\rm cm}^{-1}$ in graphite, if we change the laser excitation energy ($E_{\rm laser}$), we should be able to reproduce the phonon dispersion relations of graphite, as described by Saito et al. [9]. The two allowed double resonance processes in Ref. 9 correspond to $|q| \simeq 0$ and $|q| \simeq 2|k|$, where q and k denote, respectively, the phonon and electron wave vectors measured from the Γ and K points. The wave vectors $|q| \simeq 0$ do not depend on $E_{\rm laser}$, while the wave vectors $|q| \simeq 2|k|$ vary significantly with $E_{\rm laser}$ in order to satisfy the double resonance condition.[9] From the known dispersion relations for graphite $\omega(q)$ [see Fig. 3(a)], we see that the phonon branch oTO, which is responsible for this mode, decreases in frequency as q moves away from the Γ-point. We should therefore expect that the M band would have two components: a lower frequency component, ω_M^-, which is associated with the $|q| \simeq 2|k|$ double resonance process and which decreases in frequency with increasing $E_{\rm laser}$, and a higher frequency component, ω_M^+, which is associated with the $|q| \simeq 0$ double resonance process, and ω_M^+ is independent of $E_{\rm laser}$, in agreement with the experimental observations for ω_M^+ and ω_M^- in Fig. 2.

In Fig. 3(b) we plot the experimental results of Fig. 2 for the feature observed near $1750\,{\rm cm}^{-1}$ in SWNT bundles as a function of $E_{\rm laser}$ (lower scale), using (□) for ω_M^+ and (△) for ω_M^-. Using the upper scale in Fig. 3(b), we plot the $|q| \simeq 2|k|$ values for the M^- and LOLA bands (the upper scale does not apply to ω_M^+, where $q \simeq 0$), corresponding to a given $E_{\rm laser}$ (see Ref. 9). The connection between the two scales in Fig. 3(b) (lower $E_{\rm laser}$ and upper q) follows from the linear relation between $E_{\rm laser}$ and q, namely $E_{\rm laser} = (\sqrt{3}/2)\gamma_0 aq$, which in turn comes from the electron dispersion relation around the K-point and the double resonance condition $|q| \simeq 2|k|$. For comparison, we plot the frequencies (solid lines) according to predictions from double resonance theory for the two $\omega_M^{\pm}$ branches. The theoretical curves for ω_M^- and ω_M^+ in Fig. 3(b) are upshifted by $20\,{\rm cm}^{-1}$, as discussed below, to match the experimental observations of $\omega_M^{\pm}$ for SWNT bundles. Note that, except for the $20\,{\rm cm}^{-1}$ constant upshift of the theoretical $M^{\pm}$ dispersion curves, the agreement between theoretical predictions for ω_M^- and ω_M^+ and the experimental observations is very good. Both experimental and theoretical values exhibit the same dispersion for the M^- feature, and the same magnitude of the $\Delta\omega_M \sim 20\,{\rm cm}^{-1}$ splitting that is observed for all samples in Fig. 1 (see Table I). Also plotted in Fig. 3(b) are the points observed for $\omega_M^{\pm}$ for HOPG at $E_{\rm laser} = 2.41\,{\rm eV}$ (denoted by a filled square and a filled triangle) which are seen to be upshifted by $20\,{\rm cm}^{-1}$ from the $\omega_M^{\pm}$ observed for the SWNT bundles. However, the splitting $\Delta\omega_M$ between ω_M^- and ω_M^+ is the same for SWNT bundles, HOPG, and in the theory.

The calculated ω_M^+ and ω_M^- as a function of $E_{\rm laser}$ in Fig. 3(b) show that $\Delta\omega_M = \omega_{M^+} - \omega_{M^-} \simeq 20\,{\rm cm}^{-1}$ for $E_{\rm laser} = 2.41\,{\rm eV}$, in good agreement with experiment, but Fig. 3(b) also predicts that $\Delta\omega_M$ increases with increasing $E_{\rm laser}$. Raman spectra for irradiated graphite [13] using $E_{\rm laser} = 5.0\,{\rm eV}$ (248 nm) show two features in the frequency range of the M band, with an estimated splitting of $\Delta\omega_M \sim 60\,{\rm cm}^{-1}$. Using published force constant models [9, 11], $\Delta\omega_M$ at $E_{\rm laser} = 5.0\,{\rm eV}$ ($q = 0.53K$) can be estimated, yielding $\Delta\omega_M \sim 96\,{\rm cm}^{-1}$ for the force constants used in Ref. 9 which does not include double resonance Raman data and $\Delta\omega_M \sim 148\,{\rm cm}^{-1}$ for the force constants used in Ref. 11 based on double resonance Raman data, but does not include data for the Raman M bands in the force constant fitting procedure. At present the force constant models are not sufficiently accurate to predict $\Delta\omega_M$ for such large q values (or $E_{\rm laser}$ values as large as 5.0 eV). The two force constant models (Refs. 9, 11), which are based on fitting two rather different sets of experimental data, show large differences in their predictions of $\Delta\omega_M$ at 5.0 eV. Further improvements in the force constant models (perhaps using $\Delta\omega_M$ data for fitting inputs) are needed to fit the $\Delta\omega_M$ dispersion at large $E_{\rm laser}$ values.

In Fig. 3(b) we also plot the frequencies for the combination of the longitudinal optical mode (LO) and the longitudinal acoustic mode (LA), as predicted by double resonance theory (dark solid line) for $|q| \simeq 2|k|$. To compare these predicted values for the LO+LA frequencies, we plot in Fig. 3 the highly dispersive LOLA mode frequencies ($\diamondsuit$) observed in Fig. 2 between 1864 and 2000 ${\rm cm}^{-1}$. We see that the agreement between this observed highly dispersive LOLA mode frequency and the theoretical predictions for LO+LA is very good (thus explaining the choice of the name LOLA for this mode). Note that for this combination mode we do not expect to observe the double resonance feature related to $|q| \simeq 0$, since $\omega_{\rm LA} = 0$ and $\omega_{\rm LO} = \omega_{E_{2g}} = 1582\,{\rm cm}^{-1}$ for $|q| \simeq 0$.

Although the M features observed in SWNT bundles and in HOPG for $E_{\rm laser} = 2.41\,{\rm eV}$ are similar, there is an upshift of about $20\,{\rm cm}^{-1}$ in ω_M for HOPG compared with SWNT bundles. We attribute this difference in the observed ω_M between HOPG and SWNTs to a diameter dependent curvature effect in the cylindrical SWNTs. A related effect is observed in the G-band leading to a downshift in ω_G^-, corresponding to circumferential vibrational displacements, relative to ω_G^+ which corresponds to displacements along the SWNT axis [24, 25]. A related effect is also observed in measurements on the D and G'-band frequencies in SWNTs, for which a downshift in these mode frequencies is found to be proportional to $1/d_t$ [26–28], and this effect is discussed further below, in Sect. III C, in connection with the $M^\pm$ bands.

Also plotted in Fig. 3(b), with dotted lines, are all the other possible overtones and combination modes for two phonons associated with the Γ-point (dashed lines) and with the K-point (dotted lines) according to double resonance theory [9]. None of these other possibilities fit well to the experimental data, thus supporting the mode assignments we have used in the present work. While the double resonance theory accounts well for the behavior of the mode frequencies for $E_{\rm laser} < 3.0\,{\rm eV}$, it is interesting to note that the intensity of the double resonance Raman bands remains an open issue.

Figure 3(a) thus gives us, a more complete picture than was previously available for the phonon dispersion in graphite-like materials which can be used to interpret experimental second-order Raman spectra taken with different $E_{\rm laser}$ excitation, thereby giving more detailed information than in Ref. 9 about the various double resonance Raman processes associated with the Γ point. In particular, Fig. 3(a) includes two additional dispersion curves, one for the M feature (identified as a harmonic of the out-of-plane infrared active mode in graphite) and a second for the LOLA feature which is a combination (LO + LA) mode. Whereas previous studies were predominantly focused on double resonance effects associated with the K-point in the Brillouin zone (the D-band and the G'-band), the present work focuses on double resonance processes for non-zone center phonons connected with the Γ-point.

C. Isolated SWNTs

Figure 4 shows spectra in the 1300–2000 ${\rm cm}^{-1}$ range taken from several isolated SWNTs. These spectra all show the M band as well as the G band, and in some cases weak D-bands are also seen. For each spectrum in Fig. 4 the RBM feature was observed and the RBM frequency is given on the figure, so that (n, m) indices could be tentatively assigned to each tube, based on the RBM frequency [21] and on other diameter and chirality-dependent Raman features [18, 19, 24, 29]. From Fig. 4 we see that even though the same $E_{\rm laser}$ is used for all spectra ($E_{\rm laser} = 2.41\,{\rm eV}$), the details of the spectra of the M band at the single nanotube level vary significantly from one (n, m) nanotube to another.

Many of the nanotubes show two clear features ($\omega_M^\pm$), but some tubes show only one well-defined feature. In Fig. 4 we observe two tubes both with $\omega_{\rm RBM} = 180\,{\rm cm}^{-1}$, one showing a strong M band at $1741\,{\rm cm}^{-1}$, while the second one has a broader M band at $1753\,{\rm cm}^{-1}$ with a very different lineshape. At $\omega_{\rm RBM} \approx 130\,{\rm cm}^{-1}$, we see two tubes again with similar $\omega_{\rm RBM}$ values, and while the first has two well-defined peaks at $1738\,{\rm cm}^{-1}$ and $1768\,{\rm cm}^{-1}$, the second tube contains only one well-defined peak at $1752\,{\rm cm}^{-1}$, with a different lineshape. In these cases, tubes with similar $\omega_{\rm RBM}$ values, but with different M band features, were identified as tubes having different (n, m) values. These assignments are supported by the analysis of other diameter and chirality-dependent Raman features for these nanotubes [18, 19, 24, 29].

There are, however, other cases where tubes with approximately the same d_t also show similar M bands, as, for example, the two nanotubes with $\omega_{\rm RBM} \approx 160\,{\rm cm}^{-1}$

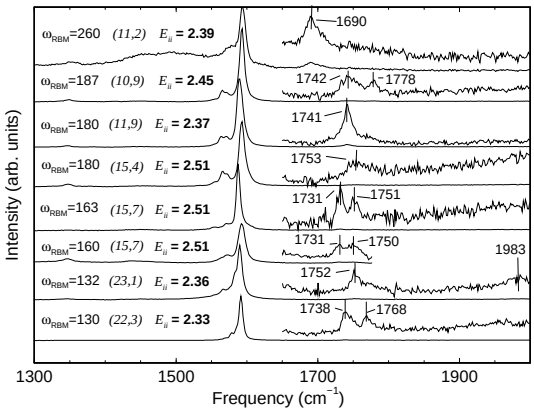

FIG. 4: Raman spectra taken with $E_{\rm laser} = 2.41\,{\rm eV}$ from several isolated SWNTs which clearly show the M band. For each tube the tentatively assigned (n, m) indices and the observed $\omega_{\rm RBM}$ and $\omega_M^{\pm}$ frequencies ($\rm cm^{-1}$) are also displayed.

where both nanotubes contain a double-featured M band at $1731\,{\rm cm}^{-1}$ and $\approx$1751 $\rm cm^{-1}$. The tubes with $\omega_{\rm RBM}$ $\approx$160 $\rm cm^{-1}$ were here tentatively assigned to the same *(n,m)* values. The assignments in this case are also supported by the similarity of other diameter and chirality-dependent Raman features for these two nanotubes [18, 19, 24, 29]. The small differences we observe comparing the two traces tentatively assigned as $(15, 7)$ SWNT in Fig. 4 are probably due to defects, as suggested by the different intensities for the D bands shown by those spectra, and may also be due to differences in the polarization of the light with respect to the tube axis (see Ref. 30).

It is interesting to note also that, at the single nanotube level, the $\Delta\omega_M \approx 20\,{\rm cm}^{-1}$ separation between the M^+ and M^- features using $E_{\rm laser} = 2.41\,{\rm eV}$ does not hold exactly, as can be seen in Fig. 4. For example, $\Delta\omega_M = 36\,{\rm cm}^{-1}$ for the SWNT tentatively assigned as $(10, 9)$, $\Delta\omega_M = 20\,{\rm cm}^{-1}$ for the $(15, 7)$ tube, and $\Delta\omega_M = 30\,{\rm cm}^{-1}$ for the (22,3) tube. However, the average value of $\Delta\omega_M$ over the 51 SWNTs is $\Delta\omega_M = 22\,{\rm cm}^{-1}$, in good agreement with the results of Fig. 2 showing $\Delta\omega_M = 23\,{\rm cm}^{-1}$ for SWNT bundles. This comparison further shows the connection between results for individual isolated SWNTs, the average of isolated SWNTs, and the corresponding results for SWNT bundles.

The dispersive feature observed in the 1950–2000 $\rm cm^{-1}$ range in SWNT bundles, as shown in Fig. 2, was rarely seen in isolated tubes due to the low intensity of this feature. For example, the spectrum assigned as $(23, 1)$ in Fig. 4, shows this feature at $1983\,{\rm cm}^{-1}$, consistent with the data for the SWNT bundles [14]. We do not have an explanation for our infrequent observation of the LOLA feature in isolated SWNTs.

Figure 5 plots ω_M (filled circles) against $(1/d_t)$, as obtained from the radial breathing mode feature $d_t = 248/\omega_{\rm RBM}$ [21], for 36 of the isolated SWNTs which contained both the M band *and* the RBM features. The open square symbols are used for the higher frequency M^+ peak in the M band when two peaks are observed. The filled square and filled triangle corresponding to $(1/d_t) = 0\,{\rm nm}^{-1}$ represent the ω_M^+ and ω_M^- frequencies observed in HOPG. No clear diameter dependence can be deduced from the data in Fig. 5, indicating that the frequencies $\omega_M^{\pm}$ for isolated SWNTs are very sensitive to chirality.

The stars (*) in Fig. 5 indicate the frequency expected at $q \sim 0$ from the combination mode $\omega_G^+ + \omega_{\rm RBM}$ for each SWNT spectrum, while the crosses ($\times$) indicate the lower frequency combination mode $\omega_G^- + \omega_{\rm RBM}$. Here ω_G^+ and ω_G^- are the frequencies of the G band peaks ($q \sim 0$) at about $1591\,{\rm cm}^{-1}$ and $1570\,{\rm cm}^{-1}$, respectively, corresponding to displacements along the tube axis (ω_G^+) and in the circumferential direction (ω_G^-).[24, 25] Figure 5 shows that the M and the RBM+G mode frequencies for some SWNTs falls in the same frequency range, but not close enough in general to explain the data points themselves. Considering the $|q| \sim 2|k|$ double resonance condition, the RBM+G modes should also vary in frequency from tube to tube, as observed for the M bands in Fig. 5, due to the different zone folding for different (n, m) nanotubes.[5] However, the RBM+G combination modes away from $q = 0$ are predicted to appear at sufficiently higher frequencies due to the positive dispersion of the acoustic branches, that it is not likely that they would interact with the M^- modes.

There is one point in Fig. 5 that is far away from the others (at $1/d_t \sim 1.1\,{\rm nm}^{-1}$). This point corresponds to the uppermost spectrum in Fig. 4 and is identified with the (11,2) SWNT. This SWNT is metallic and shows a strong M band spectral feature. The apparent difference in ω_M for this SWNT relative to all the others might be due to the fact that this SWNT exhibits a very small diameter ($d_t < 1\,{\rm nm}$), where phonons and plasmons interact strongly, thus generating an over-damped behavior, as shown by the large intensity Breit–Wigner–Fano component observed in the G^- band (see Fig. 4 and Ref. 23).

Further experimental study of such metallic tubes is indicated. From Figs. 4 and 5, we conclude that different (n, m) SWNTs show very different M bands, similar to the case of the D and G' bands in isolated SWNTs [18, 19]. These results suggest that the $M^{\pm}$ features also have a strong (n, m) dependence (including a dependence on both tube diameter and chirality), as in the case of the D and G' bands. This (n, m) dependence comes from the fact that in 1D SWNTs the double resonance conditions $q \sim 0$ and $|q| \sim 2|k|$ are limited by the possible q (and k) wave vectors that are available for this 1D system [5], and the observation of the resonance Raman effect from isolated SWNTs is further limited by the $E_{\rm laser} \sim E_{ii}$ resonance condition [21]. Unlike the situation in 2D graphite, it is not generally possible to satisfy both the resonance Raman condition and the restricted q vectors simultaneously.

Furthermore, the physics involved in the M band case seems to be more complicated than for the D and G'

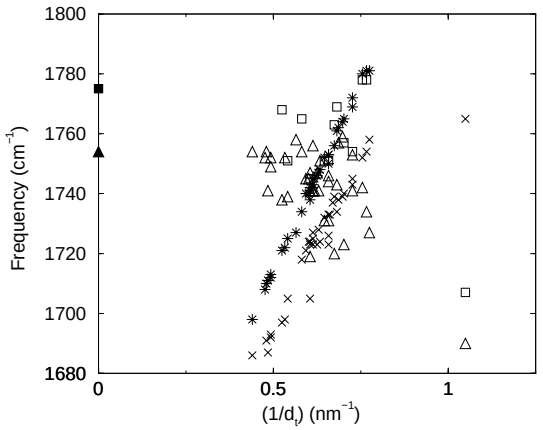

FIG. 5: Experimental M-band frequency vs. $(1/d_t)$ data points are shown as filled and open symbols. The □ are used for ω_M^+ when two features are observed and △ are used for ω_M^-. The points denoted by * indicate the frequency predicted for the $q \sim 0$ combination mode $\omega_G^+ + \omega_{\rm RBM}$, while the predicted $\omega_G^- + \omega_{\rm RBM}$ at $q \sim 0$ are denoted by × (see text). The observed M^+ and M^- data points for HOPG at $E_{\rm laser} = 2.41\,{\rm eV}$ are denoted at $(1/d_t) = 0$.

bands. In the case of the D and G' bands, it is clear which modes are involved in the process, probably because the scattering processes mediated by the D band phonons exhibit a very strong matrix element. In the case of the low intensity M and LOLA features, many overtone and combination modes [such as plasmons and the (G + RBM) combination mode] can appear in the same frequency range, as shown in Fig. 3(b) by the dotted/dashed curves (or in Fig. 5 by the * and × points), and they can be resonantly enhanced differently for different (n, m) SWNTs.

To gain insight into whether two features or one feature occur in the spectral band near $1750\,{\rm cm}^{-1}$, we plot in Fig. 6(a) the experimental frequencies ω_M against the energy of the van Hove singularity E_{ii} as calculated from (n, m) values assigned to each tube. We use the □ symbol for ω_M^+ when two features are clearly observed in the spectra, and we use the △ symbol for ω_M^-. From the 36 SWNTs that exhibit both M and RBM features, we plot here data for only the 21 SWNTs for which we can make confident (n, m) assignments; for the other 15 tubes, the quality of the other Raman features (RBM, G and G′ bands) are sufficient to determine d_t, but not good enough to obtain an unambiguous (n, m) assignment. We see that for tubes having $E_{ii} < 2.41\,{\rm eV}$, both $\omega_M^\pm$ modes are usually observed. For tubes with $E_{ii} \geq 2.41\,{\rm eV}$, only one feature (ω_M^-) is usually observed experimentally. Two M features are observed for only two SWNTs with $E_{ii} > 2.41\,{\rm eV}$, and, in both cases, the observed ω_M^+ frequencies satisfy the combination $\omega_G^+ + \omega_{RBM}$ expected according to the $\omega_{\rm RBM}$ and ω_G frequencies observed for these SWNTs. Therefore, the experimental results suggest that only one peak (M^-) is observed for $E_{ii} \geq E_{\rm laser}$, while both M^+ and M^- are observed for $E_{ii} < E_{\rm laser}$.

Figure 6(b) presents a simple model to explain the phenomena reported in Fig. 6(a), namely the existence of a threshold $E_{ii} = E_{\rm laser}$ for the appearance of the M^+ peak, that in 2D graphite corresponds to the $q \sim 0$ double resonance condition. Neglecting the trigonal warping effect [31] on a 2D graphene sheet, the equi-energy contours for an electronic state in the conduction band, resonantly excited by $E_{\rm laser}$, corresponds to a circle in k space, centered at the K point. In the case of SWNTs, the available 2D-k space is limited to the cutting lines due to the circular boundary condition along the circumference of the SWNT, and the allowed electronic states for a resonantly excited electron are represented by the crossing of the 1D cutting lines with the circle. In Fig. 6(b) we draw such an equi-energy contour for the case where E_{ii} (indicated by ×) is smaller than $E_{\rm laser}$. Only a few phonons can bring the excited electron to another real electronic state, so that the double resonance requirement can be satisfied. These phonons are explicitly indicated in the figure. Starting from a resonantly excited electronic state indicated by "1", phonon $q_{1\to2}$ brings the electron resonantly to the real state "2". In the case of a Stokes scattering process, state "2" actually corresponds to a circle of smaller radius due to the smaller energy of the scattered electron. As a first approximation, we can ignore the small change in the radius of the constant energy contour in going from state "1" to state "2", and we consider both states to be on the same circle in Fig. 6(b). This $q_{1\to2}$ phonon satisfies the double resonance requirement for $q \sim 0$. The two phonons $q_{1\to3}$ and $q_{1\to4}$ bring the electron resonantly to the real states "3" and "4", which both correspond to the double resonance requirement $|q| \sim 2|k|$.

Considering $E_{\rm laser} = 2.41\,{\rm eV}$ and $\partial\omega_M/\partial E_{\rm laser} \sim 25\,{\rm cm}^{-1}/{\rm eV}$, the difference between $q_{1\to3}$ and $q_{1\to4}$ is about $1\,{\rm cm}^{-1}$, which is too small to be resolved experimentally, so that we would expect to observe only one feature in the Raman spectra, which we have called M^-. However, $q_{1\to2}$ for $E_{\rm laser} = 2.41\,{\rm eV}$ is about $20\,{\rm cm}^{-1}$ higher than $q_{1\to3,4}$, thus allowing the M^+ peak to be distinguished from the M^- peak experimentally. It is clear that as E_{ii} approaches $E_{\rm laser}$, the state "1" approaches "2", and the state "3" approaches "4" so that the $q \sim 0$ double resonance effect disappears when "1" = "2", thus explaining the threshold at $E_{ii} = E_{\rm laser}$ for the observation of the M^+ feature.

The solid curves in Fig. 6(a) represent predicted frequencies for the processes $1 \to 2$, $1 \to 3$, and $1 \to 4$ discussed above. The phonon wavevectors $q_{1\to2}$, $q_{1\to3}$, and $q_{1\to4}$ as a function of E_{ii} are determined from a simple geometrical construction shown in Fig. 6(b). The predicted frequencies are obtained from the phonon dispersion for graphite [9] as two times the oTO mode frequency for a given phonon wavevector. The resulting predicted frequency is further upshifted by $40\,{\rm cm}^{-1}$ to satisfy experimental points shown in Fig. 6(a). Further refinements in the force constant model are needed to account for this

(a)

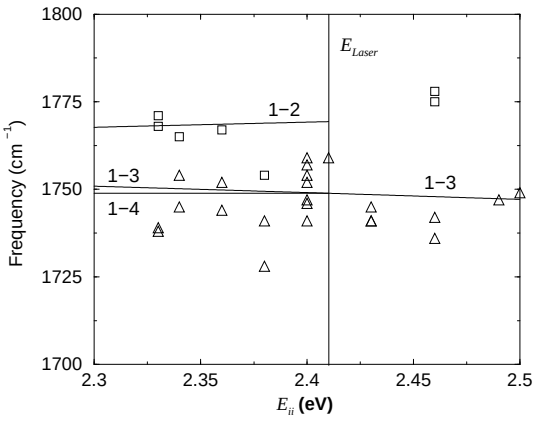

(b)

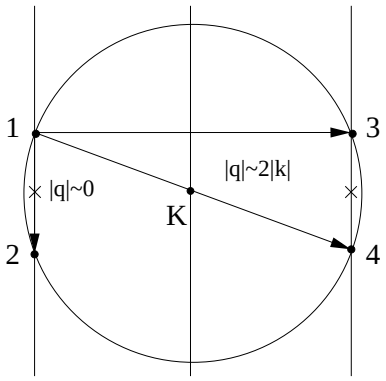

FIG. 6: (a) Frequencies for $\omega_M^-(\triangle)$ and $\omega_M^+(\square)$ observed with $E_{\rm laser} = 2.41\,{\rm eV}$ vs. the energy of the van Hove singularity in the joint density of states E_{ii} for isolated SWNTs. The solid curves are predictions for the frequencies expected from the model in (b). (b) Schematic model to explain the observation of one or two M peaks in the Raman spectra for isolated SWNTs (see text).

$40\,{\rm cm}^{-1}$ upshift in the theoretical curves.

Part of the experimentally observed upshift of the frequencies $\omega_M^{\pm}$ in graphite relative to SWNTs, comes from the dependence of these mode frequencies on nanotube diameter d_t. However, a simple plot of $\omega_M^{\pm}$ vs. $1/d_t$ for each individual SWNT would not yield a clear picture of the d_t dependence of these mode frequencies, because $\omega_M^{\pm}$ at the single nanotube level not only depends on nanotube diameter d_t, but also depends on other variables, such as nanotube curvature [expressed by (n,m)], E_{ii} and $E_{ii} - E_{\rm laser}$, and the possible interaction between ω_M^+ with various combination modes, as discussed above, and shown in Figs. 5 and 6. We have, however, found in analyzing similar effects on the single nanotube level for the D-band and G'-band features [27, 28] that when the mode frequencies are averaged over chirality, by averaging ω_D and $\omega_{G'}$ over a significant number (> 10) of SWNTs which are each resonant with a particular E_{ii} singularity, so that the SWNTs for each E_{ii} have similar values of d_t, a clear picture emerges for the dependence

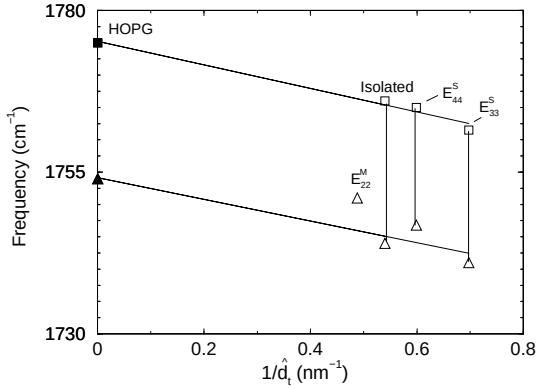

FIG. 7: Plot of the frequencies ω_M^+ and ω_M^- averaged over the E_{33}^S singularity and over the E_{44}^S singularity in the joint density of states of individual SWNTs vs. their average $1/\hat{d}_t$ values. Also included are the corresponding experimental points for HOPG ($1/d_t \to 0$). A least square fit of $\omega_M^{\pm}$ to these data points yields $\hat{\omega}_M^+ = 1775 - 18.0/\hat{d}_t$ and $\hat{\omega}_M^- = 1754 - 16.7/\hat{d}_t$. The data points labeled isolated are for an average of $\omega_M^{\pm}$ for 51 isolated nanotubes (see text). The data point E_{22}^M represents an average of ω_M^- for 3 metallic SWNTs corresponding to the E_{22}^M singularity (see text).

of ω_D and $\omega_{G'}$ on d_t. Using the same approach as for the D and G' bands, we averaged the values of $\omega_M^{\pm}$ over all the M band spectra we have available for the E_{33}^S singularity, and similarly for the E_{44}^S singularity, and we then plotted in Fig. 7 the average values thus obtained for $\hat{\omega}_M^{\pm}$ as a function of the average reciprocal diameter $1/\hat{d}_t$, including the $\omega_M^{\pm}$ values for HOPG. A least squares fit to a linear dependence $\hat{\omega}_M^{\pm} = \omega_M^{0\pm} - \beta^{\pm}/\hat{d}_t$ is then made for these three data points for ω_M^+ and for the corresponding three data points for ω_M^-, where the $\omega_M^{0\pm}$ values are chosen as the measured values in HOPG for which $1/d_t \to 0$. The results of the least squares fit to these values yields $\beta^+ = 18.0\,{\rm cm}^{-1}{\rm nm}$ and $\beta^- = 16.7\,{\rm cm}^{-1}{\rm nm}$ for the ω_M^+ and ω_M^- features, respectively. It is interesting that the values for β obtained for these two features are similar to one another, and also to the corresponding value of $16.5\,{\rm cm}^{-1}{\rm nm}$ for the d_t dependence of the D-band [27, 28]. In addition, we plot in Fig. 7 the average $\bar{\omega}_M^{\pm}$ values for 51 SWNTs, using the results from Table I, and good agreement of these points with the least squares fit in Fig. 7 is obtained. Similarly, the point labeled E_{22}^M denotes averaged data for 3 isolated metallic SWNTs in resonance with E_{22}^M, and since there are not enough data points available for obtaining a reliable average over chiral angles for E_{22}^M, this point for ω_M^- was not used in the least squares fitting procedure.

The decrease in the average $\omega_M^{\pm}$ with decreasing d_t shown in Fig. 7 can be associated with an increase in nanotube curvature and a resulting decrease in the vibrational force constants with decreasing d_t. However, for a clear identification of the mode frequencies at the single nanotube level, it is necessary to consider in detail

the dependence of $\omega_M^{\pm}$ on chirality, due to the different zone folding effects for phonons and electrons, and to differences in $E_{ii} - E_{\rm laser}$.

D. Resonance issues of SWNTs: from isolated SWNTs to SWNT bundles

It is also interesting to compare the behavior of isolated SWNTs and SWNT bundles. We see that a rich frequency and intensity behavior is observed for the different isolated (n, m) SWNTs, due to the confinement of electrons and phonons in this 1D system. However, when we average over a large number of isolated SWNTs (51 SWNTs in this work), we observe results that are consistent with SWNT bundles, and these results are basically similar to the results observed in the parent material, graphite. From the results presented in Sect. III, we see that the assignment of the M band in SWNTs to a combination of the $RBM + G$ bands is not correct, although many average results, [i.e., $\omega_M \sim \omega_{RBM+G}$ and the splitting $\Delta\omega_M \sim (\omega_{G^+} - \omega_{G^-})$ at $E_{\rm laser} = 2.41\,{\rm eV}$] are in good agreement with this assignment. Also for a few of the isolated SWNTs that we measured, the M feature appears at the same frequency as the (RBM+G) combination mode at $q \simeq 0$.

The present work shows three new features that are accounted for by the double resonance process: the M^+, M^- and LOLA features. We further expect that other, yet unassigned, Raman features observed in sp^2 graphite-like materials should be assigned using the double resonance process, considering one, two or more phonon scattering processes (see for example the spectra of Tan et al.[32] on graphite whiskers), and considering not simply the sum of $q = 0$ frequencies, but also difference frequencies in applying the double resonance conditions.

Regarding the low frequency (below $1620\,{\rm cm}^{-1}$) second-order combination of modes, we know from the literature[16] that SWNT bundles exhibit two modes that have not yet been assigned. Modes are observed at (1) $\omega_1 = 750\,{\rm cm}^{-1}$ and (2) $\omega_2 = 970\,{\rm cm}^{-1}$ (for $E_{\rm laser} = 2.41\,{\rm eV}$), and they exhibit opposite frequency dispersions: $\partial\omega_1/\partial E_{\rm laser} \sim +130\,{\rm cm}^{-1}$ and $\partial\omega_2/\partial E_{\rm laser} \sim -130\,{\rm cm}^{-1}$.[16] These features have not been observed in HOPG, but have only been seen in SWNT bundles. Considering all the branches in the Brillouin zone of 2D graphite, there is no second-order combination of modes that come from either the Γ or the K points that explain this feature. However, if difference frequencies are also considered, an assignment can be made as follows. We tentatively assign the ω_1 feature in Ref. 16 to the combination of the following two modes. The first phonon is iTA at the Γ point, $|q| = 2|k|$, emission, and the second phonon is oTA (or oTO) at the K point, $q = 0$, emission. For the feature ω_2 in Ref. 16, we assign the first phonon to iTA at the Γ point, $|q| = 2|k|$, absorption, and the second phonon to LA at the K-point, $q = 0$, emission. Using the set of force constants from Grüneis et al.[11], we calculated the expected ω_1 and ω_2 as well as $\partial\omega_1/\partial E_{\rm laser}$ and $\partial\omega_2/\partial E_{\rm laser}$ at $E_{\rm laser} = 2.41\,{\rm eV}$, according to double resonance theory. Since the second phonon is not dispersive ($q = 0$), the dispersion for both ω_1 and ω_2 is given by the slope of the iTA mode, which is opposite for absorption and emission so that $|\partial\omega_{\rm iTA}/\partial E_{\rm laser}| = 127\,{\rm cm}^{-1}/{\rm eV}$, and the double resonance process gives $\partial\omega_1/\partial E_{\rm laser} = -127{\rm cm}^{-1}/{\rm eV}$ and $\partial\omega_2/\partial E_{\rm laser} = +127\,{\rm cm}^{-1}/{\rm eV}$, in good agreement with observations [16]. From Ref. 11, the expected frequencies for $E_{\rm laser} = 2.41\,{\rm eV}$ are: $\omega_{\rm iTA}(\Gamma, |q| = 0.23K) = 305\,{\rm cm}^{-1}$, $\omega_{\rm oTA}(K, q = 0) = 577\,{\rm cm}^{-1}$, and $\omega_{\rm LA}(K, q = 0) = 1054\,{\rm cm}^{-1}$, which gives us $\omega_1 = 749\,{\rm cm}^{-1}$ and $\omega_2 = 882\,{\rm cm}^{-1}$. Thus, ω_1 is in excellent agreement with experiment, but ω_2 is downshifted by $90\,{\rm cm}^{-1}$. This may be due to an inaccuracy in the oTA frequency at the K point in the force constant model. For example, Raman and infra-red data are plotted for the oTO mode near the K point [33, 34]. According to these data, $\omega_{\rm oTO}(K, q = 0) \sim 635\,{\rm cm}^{-1}$. If we use the oTA instead of the oTO mode value at the K-point, we get $\omega_2 = 940\,{\rm cm}^{-1}$, which is $30\,{\rm cm}^{-1}$ lower than the observed experimental value,[16, 35]. Further refinement of this tentative assignment is needed.

It is interesting to note that a combination of modes involving both the emission and absorption of phonons are commonly observed in molecules such as SO_2 [36, 37]. It is important to stress that, in both cases, the combination modes tentatively assigned to account for the two features observed by Alvarez et al.[16] involves one phonon from close to the Γ point and one from close to the K point. Due to momentum conservation, this combination is not possible in graphite, unless it is a third-order process involving a defect-induced scattering. In the case of SWNTs, such a process might be possible because of zone folding.

IV. CONCLUSION

In this paper, we present an advance in our understanding of the phonon dispersion relations in graphite-like materials which can be used to interpret experimental second-order Raman spectra taken with different laser excitation energies, thereby giving more detailed information than in Ref. 9 about the various double resonance Raman processes associated with the Γ point. We expect that other Raman features observed in sp^2 graphite-like materials will in the future be identified in terms of the double resonance process, considering one, two or more phonon scattering processes, and including combinations of both sums and differences of phonon mode frequencies.

From another point of view, the results presented here show that we can use resonance Raman spectroscopy measurements to determine the phonon dispersion relations of graphite and graphite-related materials associated with combination modes and overtones of the sp^2 carbon phonon modes with non-zone-center or zone edge

wavevectors in the Brillouin zone of graphite. In this work the M^+, M^- and LOLA features are identified and can be used to fit phonon dispersion curves in the future [11].

In the case of SWNTs, these second-order overtones and combination bands are found to vary from tube to tube, suggesting a dependence of these spectral features, at the single nanotube level, on tube diameter, chirality, and on E_{ii} values associated with the one-dimensional SWNT electronic and phonon dispersion relations. Furthermore, the experimental results indicate that the resonance condition, i.e., the energy position of $E_{\rm laser}$ with respect to E_{ii}, is also important in the double resonance process in 1D systems. For example, the M^+ feature is only observed for SWNTs with $E_{ii} < E_{\rm laser}$ and on the basis of the possible phonon scattering processes, we propose a qualitative model to explain this result. Furthermore, we observed modes that can be assigned as the coupling between Γ and K-point phonons. Detailed calculations are needed to fully understand these results.

It is also shown that when we average over a large number of isolated SWNTs we observe results that are consistent with SWNT bundles, and these results are basically similar to the results observed in the parent material, graphite, and the frequency dispersion can be explained by a double resonance theory considering two-dimensional graphite structure.

The zone folding of the 2D graphene Brillouin zone into the 1D SWNT Brillouin zone makes it possible to observe the combination of many other phonon features in the interior of the 2D graphite Brillouin zone. The crossing of the possible wave vectors q and k with cutting lines of allowed discrete 1D q and k values for SWNTs needs to be taken into account.

Acknowledgments

The authors acknowledge Dr. S.D.M. Brown for providing experimental data that were used in this study. V.W.B. thanks the Lord Foundation for its support of his undergraduate research project. A.J. and A.G.S.F. acknowledge financial support from the Brazilian agency CNPq. The experimental work was performed at Boston University at the Photonics Center, operated in conjunction with their Department of Physics and the Department of Electrical and Computer Engineering. The MIT authors acknowledge support under NSF Grants DMR 01-16042, INT 98-15744, and INT 00-00408. R.S. acknowledges a Grant-in-Aid (No. 13440091) from the Ministry of Education, Japan.

[1] M. S. Dresselhaus, G. Dresselhaus, K. Sugihara, I. L. Spain, and H. A. Goldberg, *Graphite Fibers and Filaments* (Springer-Verlag, Berlin, 1988), Vol. 5 of *Springer Series in Materials Science*.

[2] Olle Ingan and Ingemar Lundst, Science **284**, 1281–1282 (1999).

[3] J. H. Hafner, C. L. Cheung, and C. M. Lieber, Nature **398**, 761 (1999).

[4] W. A. de Heer, W. S. Bacsa, A. Châtelain, T. Gerfin, R. Humphrey-Baker, L. Forró, and D. Ugarte, Science **268**, 845 (1995).

[5] R. Saito, G. Dresselhaus, and M. S. Dresselhaus, *Physical Properties of Carbon Nanotubes* (Imperial College Press, London, 1998).

[6] M. S. Dresselhaus, G. Dresselhaus, and Ph. Avouris, *Carbon Nanotubes: Synthesis, Structure, Properties and Applications* (Springer-Verlag, Berlin, 2001), Vol. 80 of *Springer Series in Topics in Appl. Phys.*

[7] M. S. Dresselhaus and P. C. Eklund, Advances in Physics **49**, 705–814 (2000).

[8] A. M. Rao, E. Richter, S. Bandow, B. Chase, P. C. Eklund, K. W. Williams, M. Menon, K. R. Subbaswamy, A. Thess, R. E. Smalley, G. Dresselhaus, and M. S. Dresselhaus, Science **275**, 187–191 (1997).

[9] R. Saito, A. Jorio, A. G. Souza Filho, G. Dresselhaus, M. S. Dresselhaus, and M. A. Pimenta, Phys. Rev. Lett. **88**, 027401 (2002).

[10] C. Thomsen and S. Reich, Phys. Rev. Lett. **85**, 5214 (2000).

[11] A. Grüneis, R. Saito, T. Kimura, L. G. Cançado, M. A. Pimenta, A. Jorio, A. G. Souza Filho, G. Dresselhaus, and M. S. Dresselhaus, Phys. Rev. B page in press (2002). submitted 12/14/01: MS BM8175; accepted 1/18/02.

[12] Y. Kawashima and G. Katagiri, Phys. Rev. B **52**, 14 (1995).

[13] M. Bonelli, A. Miotello, P. M. Ossi, A. Pessi, and S. Gialanella, Phys. Rev. B **59**, 13513 (1999).

[14] S. D. M. Brown, A. Jorio, G. Dresselhaus, and M. S. Dresselhaus, Phys. Rev. B **64**, 073403–1 – 073403–4 (2001).

[15] Y. Kawashima and G. Katagiri, Phys. Rev. B **59**, 62–64 (1999).

[16] L. Alvarez, A. Righi, S. Rols, E. Anglaret, and J. L. Sauvajol, Chem. Phys. Lett. **320**, 441–447 (2000).

[17] S. D. M. Brown, P. Corio, A. Marucci, M. A. Pimenta, M. S. Dresselhaus, and G. Dresselhaus, Phys. Rev. B **61**, 7734–7742 (March 2000).

[18] A. G. Souza Filho, A. Jorio, G. Dresselhaus, M. S. Dresselhaus, R. Saito, A. K. Swan, M. S. Ünlü, B. B. Goldberg, J. H. Hafner, C. M. Lieber, and M. A. Pimenta, Phys. Rev. B **65**, 035404–1 – 035404–6 (2002).

[19] A. G. Souza Filho, A. Jorio, G. Dresselhaus, M. S. Dresselhaus, Anna K. Swan, M. S. Ünlü, B. B. Goldberg, R. Saito, J. H. Hafner, C. M. Lieber, and M. A. Pimenta, Phys. Rev. B **65**, 085417 (2002).

[20] J. H. Hafner, C. L. Cheung, T. H. Oosterkamp, and C. M. Lieber, J. Phys. Chem. B **105**, 743 (2001).

[21] A. Jorio, R. Saito, J. H. Hafner, C. M. Lieber, M. Hunter, T. McClure, G. Dresselhaus, and M. S. Dresselhaus, Phys. Rev. Lett. **86**, 1118–1121 (2001).

[22] M. A. Pimenta, A. Marucci, S. Empedocles, M. Bawendi, E. B. Hanlon, A. M. Rao, P. C. Eklund, R. E. Smalley,

G. Dresselhaus, and M. S. Dresselhaus, Phys. Rev. B Rapid **58**, R16016–R16019 (1998).

[23] A. Jorio, A. G. Souza Filho, V. W. Brar, Ge. G. Samsonidze, G. Dresselhaus, M. S. Dresselhaus, A. K. Swan, M. S. Ünlü, B. B. Goldberg, and R. Saito, Phys. Rev. B (2002). to be submitted.

[24] A. Jorio, A. G. Souza Filho, G. Dresselhaus, M. S. Dresselhaus, A. K. Swan, B. Goldberg, M. S. Ünlü, M. A. Pimenta, J. H. Hafner, C. M. Lieber, and R. Saito, Phys. Rev. B (2002). BF8180; submitted 6/14/01: resubmitted 10/13/01: reresubmitted 1/9/02; accepted 1/22/02.

[25] R. Saito, T. Takeya, T. Kimura, G. Dresselhaus, and M. S. Dresselhaus, Phys. Rev. B **57**, 4145–4153 (1998).

[26] M. A. Pimenta, A. Jorio, S. D. M. Brown, A. G. Souza Filho, G. Dresselhaus, J. H. Hafner, C. M. Lieber, R. Saito, and M. S. Dresselhaus, Phys. Rev. B **64**, 041401–1–041401–4 (2001).

[27] A. G. Souza Filho, A. Jorio, Ge. G. Samsonidze, G. Dresselhaus, M. S. Dresselhaus, R. Saito, and M. A. Pimenta, (2002). unpublished.

[28] A. G. Souza Filho. *Raman in SWNTs*. Ph. D. thesis, Universidade Federal do Ceará, Fortaleza-CE, 60455-760, Brazil, Departamento de Física, December 2001.

[29] R. Saito, A. Jorio, J. H. Hafner, C. M. Lieber, M. Hunter, T. McClure, G. Dresselhaus, and M. S. Dresselhaus, Phys. Rev. B **64**, 085312–085319 (2001).

[30] A. Jorio, A. G. Souza Filho, V. W. Brar, A. K. Swan, M. S. Ünlü, B. B. Goldberg, A. Righi, J. H. Hafner, C. M. Lieber, R. Saito, G. Dresselhaus, and M. S. Dresselhaus, Phys. Rev. B Rapid page in press (2002). 7/31/01 submitted: 1/03/02 approved for publication: MS BGR859.

[31] R. Saito, G. Dresselhaus, and M. S. Dresselhaus, Phys. Rev. B **61**, 2981–2990 (2000).

[32] P. H. Tan, C. Y. Hu, J. Dong, W. C. Shen, and B. F. Zhang, Phys. Rev. B **64**, 214301 (2001).

[33] G. Kern. *Clean and hydrogenated diamond and graphite surfaces*. PhD thesis, Technische Universit at Wien (1998), 1998. Department of Physics.

[34] G. Benedek, F̃. Hofman, P. Ruggerone, G. Onida, and L. Miglio, Surf. Sci. Rep. **20**, 1 (1994).

[35] L. Alvarez, A. Righi, T. Guillard, S. Rols, E. Anglaret, D. Laplaze, and J.-L. Sauvajol, Chem. Phys. Lett. **316**, 186–190 (2000).

[36] A. S. Pine, G. Dresselhaus, B. J. Palm, R. W. Davies, and S. A. Clough, J. Molec. Spectrosc. **67**, 386 (1977).

[37] Gerhard F. Herzberg, in *Infrared and Raman Spectra of Polyatomic Molecules*, (Van Nostrand Reinhold, New York, 1949).